Prediction of the Next Solar Rotation Synoptic Maps Using an Artificial Intelligence–based Surface Flux Transport Model

Hyun-Jin Jeong[1,2] , Mingyu Jeon[2] , Daeil Kim[2] , Youngjae Kim[2] , Ji-Hye Baek[3,4] , Yong-Jae Moon[2,5] , and Seonghwan Choi[3,4]

[1] Centre for mathematical Plasma Astrophysics, Department of Mathematics, KU Leuven, Celestijnenlaan 200B, 3001 Leuven, Belgium; jeong_hj@khu.ac.kr
[2] School of Space Research, Kyung Hee University, Yongin, 17104, Republic of Korea; moonyj@khu.ac.kr
[3] Technology Center for Astronomy and Space Science, Korea Astronomy and Space Science Institute, Daejeon, 34055, Republic of Korea
[4] Space Science Division, Korea Astronomy and Space Science Institute, Korea Astronomy and Space Science Institute, Daejeon, 34055, Republic of Korea
[5] Department of Astronomy and Space Science, College of Applied Science, Kyung Hee University, Yongin, 17104, Republic of Korea

Abstract

In this study, we develop an artificial intelligence (AI)-based solar surface flux transport (SFT) model. We predict synoptic maps for the next solar rotation (27.2753 days) using deep learning. Our model takes the latest synoptic maps and their sine-latitude grid data as inputs. Synoptic maps, which represent global magnetic field distributions on the solar surface, have been widely used as initial boundary conditions in the Sun and space-weather prediction models. Here we train and evaluate our deep-learning model, based on the Pix2PixCC architecture, using data sets of Solar Dynamics Observatory/Helioseismic and Magnetic Imager, Solar and Heliospheric Observatory/ Michelson Doppler Imager, and National Solar Observatory/Global Oscillation Network Group synoptic maps with a resolution of 360 by 180 (longitude and sine latitude) from 1996 to 2023. We present results of our model and compare them with those from the persistent model and the conventional SFT model, including the effects of differential rotation, meridional flow, and diffusion on the solar surface. The average pixel-to-pixel correlation coefficient between the target and our AI-generated data, after 10 by 10 binning with a $10°$ resolution in longitude, is 0.71. This result is qualitatively similar to the results of the conventional SFT model (0.65–0.68) and better than the results of the persistent model (0.56). Our model successfully generates magnetic features, such as the diffusion of solar active regions and the motions of supergranules. Using synthetic input data with bipolar structures, we confirm that our model successfully reproduces differential rotation and meridional flow. Finally, we discuss the advantages and limitations of our model in view of magnetic field evolution and its potential applications.

1. Introduction

Magnetic fields on the solar surface play a crucial role in shaping the large-scale structure of the Sun's atmosphere and driving space-weather disturbances that affect Earth's environment (D. H. Mackay & A. R. Yeates 2012; D. Nandy et al. 2023). Various numerical schemes for predicting the solar corona and space weather have used global solar photospheric magnetic field data as model inputs (M. J. Owens et al. 2014). The global photospheric field data are routinely provided as synoptic maps, produced by merging a series of line-of-sight full-disk magnetograms over a solar synodic rotation period of 27.2753 days (referred to as a Carrington rotation or CR). For each magnetogram, the data within a certain longitudinal range of the central meridian are used to construct the synoptic maps (R. Howard et al. 1969; J. T. Hoeksema & P. H. Scherrer 1986). The synoptic maps, available over several decades, have facilitated understanding of the evolution and transport of solar magnetic flux on timescales ranging from a solar rotation to solar cycles (L. E. A. Vieira & S. K. Solanki 2010; S. Gosain et al. 2013).

The surface flux transport (SFT) model has been used to predict the distribution of the Sun's magnetic fields and has

been shown to provide a good description of the global evolution after magnetic field emergence (R. H. Cameron et al. 2012). The conventional SFT model is based on the idea that radial magnetic flux on the solar surface is transported by horizontal plasma flow but without any back-reaction on these flows (R. B. Leighton 1964). Accurate modeling of SFT requires observationally constrained descriptions of large-scale flow parameters, such as differential rotation, meridional circulation, and supergranular diffusion. On the solar surface, equatorial regions rotate faster than polar regions. Poleward meridional circulation drives the polarity reversal of the solar magnetic fields. Magnetic field diffusion is generated by the random motions of supergranules on the solar surface. Each SFT parameter has been empirically determined based on long-term photospheric observations, and the model results are highly dependent on their values (T. Whitbread et al. 2017).

Deep learning, also broadly known as artificial intelligence (AI), has been used to predict magnetic fields on the solar surface. L. Bai et al. (2021) predicted the evolution of a solar active region's magnetic fields over the next 6 hr using a 12 hr sequence of Spaceweather HMI Active Region Patch data sets with a spatiotemporal long short-term memory network. F. P. Ramunno et al. (2024) predicted the next 24 hr of solar full-disk magnetograms using Solar Dynamics Observatory (SDO)/Helioseismic and Magnetic Imager (HMI) data sets with a denoising diffusion probabilistic model. However, it has been challenging to compare global magnetic flux transport
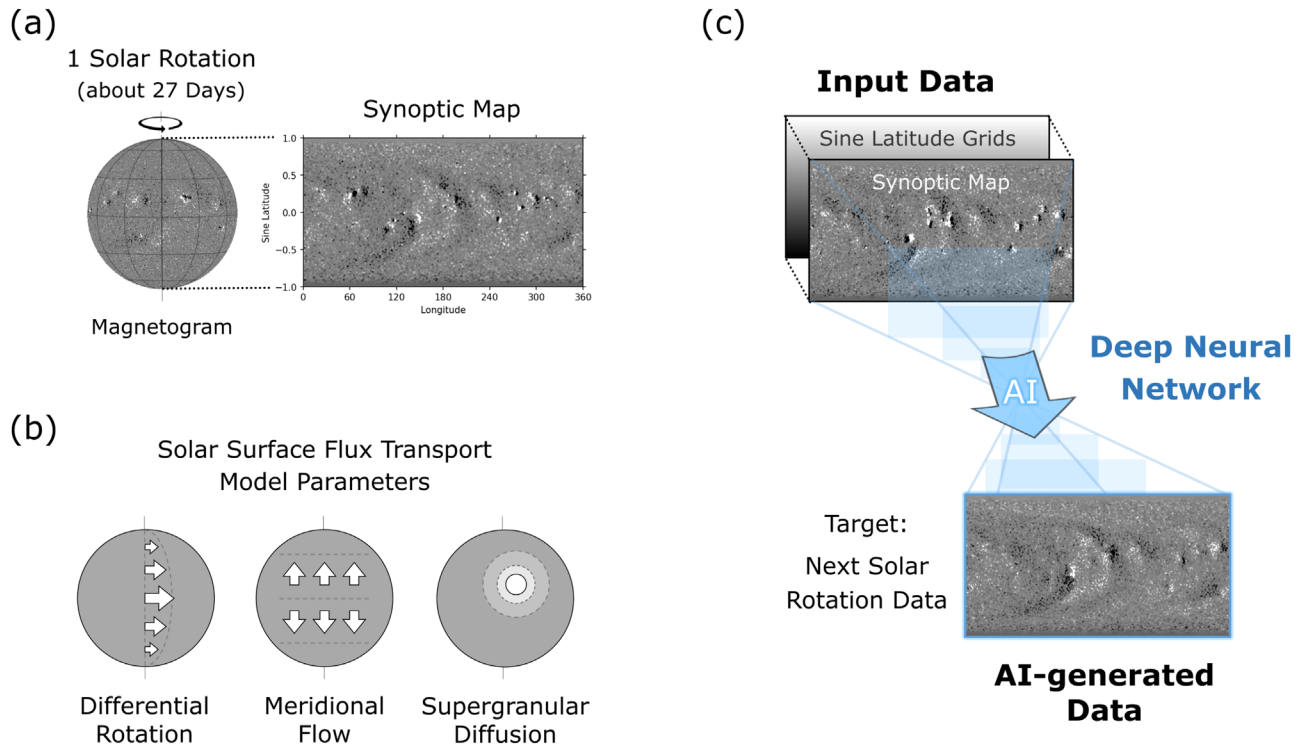
Figure 1. Overview of the conventional synoptic map and SFT model parameters, and our proposed approaches to predict the next solar rotation magnetic fields. (a) A synoptic map is constructed from magnetic field data near the Sun's central meridian over a solar rotation. (b) The conventional surface flux transport model, describing the long-term evolution of the photospheric magnetic fields, includes differential rotation, meridional flow, and supergranular diffusion. (c) Our deep neural network generates the next solar rotation photospheric field data from the latest synoptic map and its sine-latitude grid data.

between the results of the conventional SFT model and AI-based prediction models when using local or full-disk magnetic field predictions with several-hour-ahead results. J. J. Athalathil et al. (2024) used a physics-informed neural network–based model to study the evolution of bipolar magnetic regions, aiming to enhance computational accuracy in simulating SFT equations on the solar surface by overcoming the challenges of conventional grid-based methods. However, their model did not incorporate observed data for training, and they planed to use real magnetic field data in future studies.

In the present study, we propose a data-driven AI-based SFT model to predict the evolution of global magnetic fields on the solar surface during a solar rotation. We use synoptic maps and their sine-latitude grid data as the model input, and the next solar rotation synoptic maps as the model output. Our AI-based SFT model is based on the Pix2PixCC architecture, which can generate realistic magnetic field data without any artificial saturation limits from the model inputs (H.-J. Jeong et al. 2022). Figure 1 shows the construction of a synoptic map, three main parameters of the conventional SFT model, and our AI-based SFT model's input and output data configurations. We describe our data configurations in Section 2 and model structures in Section 3. We show the evaluation metric results of our AI-based SFT model and compare our model results with those from the persistent model and the conventional SFT models in Section 4. We summarize and conclude our study in Section 5.

2. Data

Here we use Solar and Heliospheric Observatory (SOHO)/ Michelson Doppler Imager (MDI) synoptic maps from 1996 June to 2010 November, SDO/HMI synoptic maps from 2010 May to 2023 December, and National Solar Observatory (NSO)/Global Oscillation Network Group (GONG) synoptic maps from 2006 August to 2023 December to train and evaluate our deep-learning model. Polar fields that are missing or of poor quality from HMI and MDI synoptic maps are filled using a two-dimensional spatial–temporal interpolation correction scheme from X. Sun et al. (2011) and those from GONG synoptic maps are filled using a cubic polynomial surface fit to the currently observed magnetic fields at neighboring latitudes. The full CR HMI, MDI, and GONG synoptic maps have resolutions of 3600×1440, 3600×1080, and 360×180, equally spaced in longitude and sine latitude, respectively. We interpolate all maps to a uniform 360×180 grid in longitude and sine latitude without applying cross calibrations. We make them 512×256 data for computation by adding proper padding (same data for the left and right sides, and reflected data for the upper and lower sides), considering the spherical surface. For the model evaluation, we use 360×180 data extracted from the 512×256 model input and output corresponding to the synoptic maps. The resolution of our model input and output is approximately $11''$ per pixel.

For this study, we collected 592 synoptic maps from CR 1910 to CR 2279, including data from solar cycles 23 and 24 and data from the ascending phase of solar cycle 25, to train, validate, and test our model. Since the number of synoptic maps is insufficient, we augment the training data set approximately 360 times by shifting $1°$ in longitude to provide a more diverse data set during training (C. Shorten & T. M. Khoshgoftaar 2019; S. Rahman et al. 2023). Data augmentation is not applied to the validation and test data sets. We use pairs of synoptic maps and their sine-latitude grid data as the input and the next solar rotation synoptic maps as the

output of our model, ensuring no duplication between the training, validation, and test data sets. We consider two consecutive years for training, six consecutive months for validation, and six consecutive months for testing from 1996 June to 2023 December. To ensure that our model's performance is generalized and not limited to specific data sets, we employ K-fold cross validation with six folds ($K = 6$), enabling the entire set of synoptic maps to be used for testing. We train our model six times with different data splits and report the averaged metric results from the six trained models. For each fold iteration, we take approximately 90,000 (multiplied by 360), 100, and 100 pairs for the training, validation, and test data sets, respectively.

3. Methods

3.1. Conventional SFT Model

The conventional SFT model describes the passive transport of radial magnetic fields (B_r) on the solar surface under the effects of differential rotation, meridional flow, and supergranular diffusion as shown in Figure 1(b). In this study, we use empirical parameters and the equation of the conventional SFT model (A. R. Yeates et al. 2023):

$$\frac{\partial B_r}{\partial t} = -\Omega(\theta)\frac{\partial B_r}{\partial \phi} - \frac{1}{R_\odot \sin\theta}\frac{\partial}{\partial \theta}[u(\theta)B_r \sin\theta] + \eta_H$$
$$\times \left[\frac{1}{R_\odot^2 \sin\theta}\frac{\partial}{\partial \theta}\left(\sin\theta\frac{\partial B_r}{\partial \theta}\right) + \frac{1}{R_\odot^2 \sin^2\theta}\frac{\partial^2 B_r}{\partial \phi^2}\right], \quad (1)$$

where ϕ, θ, $R_\odot$, $\Omega(\theta)$, $u(\theta)$, and η_H represent the longitude, latitude, solar radius, differential rotation, meridional circulation, and horizontal diffusion, respectively. The equation is derived from the radial component of the mean-field magnetohydrodynamic induction equation at the solar surface, assuming that the field at the surface is purely vertical (J. Jiang et al. 2014). We use an empirically derived velocity profile for the differential rotation as determined by H. B. Snodgrass & R. K. Ulrich (1990): $\Omega(\theta) = 0.18 - 2.396\cos^2\theta - 1.787\cos^4\theta$, where $\Omega(\theta)$ is expressed in units of degrees per day. The constant term in the differential rotation profile is provided in the Carrington frame, which is commonly used in conventional SFT models. For the meridional flow, we use the profile $u(\theta) = -R_\odot \Delta_u \cos\theta \sin^p\theta$, where Δ_u represents the flow divergence at the solar equator. For this study, we adopt $\Delta_u = 6.9 \times 10^{-8}\,\mathrm{s}^{-1}$, $p = 3.87$, and $\eta_H = 425\,\mathrm{km}^2\,\mathrm{s}^{-1}$. For more details, refer to A. R. Yeates et al. (2023); its baseline code is available at https://github.com/antyeates1983/sft_data.

3.2. AI-based SFT Model

We employ a deep-learning model based on the Pix2PixCC, as illustrated in Figure 2. Our model consists of three major components: a generator, a discriminator, and an inspector. The generator aims to produce target-like outputs from inputs, guided by objective functions from the discriminator and the inspector during the training. In this study, we replace the generator of the Pix2PixCC proposed by H.-J. Jeong et al. (2022) with the U-Net. The U-Net features a symmetric U-shaped architecture, consisting of encoder convolutional layers and decoder transposed convolutional layers, connected by skip connections (O. Ronneberger et al. 2015). Skip connections provide detailed features from previous encoder

layers to decoder layers, enabling the generation of more precise and representative outputs. The U-Net with skip connections is widely used in video frame prediction tasks (Y. Qiang et al. 2020; B. Q. Bastos et al. 2021), and has been applied to predict the global total electron content of the ionosphere for one-day space-weather forecasting (S. Lee et al. 2021). The discriminator distinguishes between real pairs (input and target data) and generated pairs (input and the generator output), and the inspector calculates correlation coefficients (CCs) between targets and the generator outputs to improve the consistency between target and output.

The discriminator extracts features via convolutional layers, enabling the calculation of a feature-matching loss ($\mathcal{L}_{FM}$), which optimizes the generator. Unlike direct data differences, $\mathcal{L}_{FM}$ minimizes the discrepancy between feature maps of real and generated pairs. This approach is particularly effective for handling data with a broad dynamic range (A. Rana et al. 2019; D. Marnerides et al. 2021):

$$\mathcal{L}_{FM}(G, D) = \sum_{i=1}^{T}\frac{1}{N_i}\|D^{(i)}(x, y) - D^{(i)}(x, G(x))\|, \quad (2)$$

where G, D, T, i, N_i, x, and y denote the generator, the discriminator, the total number of layers, the serial number of the layers, the number of elements in output feature maps of each layer, the input data, and the target data, respectively. $D^{(i)}$ represents the ith layer of D, and $G(x)$ is the generator's output.

For the adversarial process to produce realistic outputs, we adopt the least-squares generative adversarial network (LSGAN) losses (X. Mao et al. 2017), defined as

$$\mathcal{L}_{LSGAN}^G(G, D) = \frac{1}{2}(D(x, G(x)) - 1)^2$$
$$\mathcal{L}_{LSGAN}^D(G, D) = \frac{1}{2}(D(x, y) - 1)^2 + \frac{1}{2}(D(x, G(x)))^2, \quad (3)$$

where $D(x, G(x))$ and $D(x, y)$ represent probabilities ranging from 0 (generated) to 1 (real), computed by the discriminator for generated and real pairs, respectively. The generator minimizes the $\mathcal{L}_{LSGAN}^G$, while the discriminator minimizes $\mathcal{L}_{LSGAN}^D$. The competition between the generator and the discriminator contributes to generating realistic outputs. The performance of adversarial objectives has been well demonstrated in image-to-image translation tasks for solar data (E. Park et al. 2019; H.-J. Jeong et al. 2020, 2022).

To stabilize training, we adopt a CC loss ($\mathcal{L}_{CC}$) based on Lin's concordance CC (L. I.-K. Lin 1989), which balances positive and negative polarity fields better than error-based losses (R. Vallejos et al. 2020; B. T. Atmaja & M. Akagi 2021). The $\mathcal{L}_{CC}$, computed at multiple scales, is expressed as

$$\mathcal{L}_{CC}(G) = \sum_{i=0}^{T}\frac{1}{T+1}(1 - CC_i(y, G(x))), \quad (4)$$

where T and i denote the total number of downsampling by a factor of 2 and the serial number of the downsampling, respectively. CC_i indicates the CC value between the 2^i times downsampled target and generated data. The average of the CC values from multiscale targets and AI-generated results guides the model in optimizing its parameters. In addition, with the
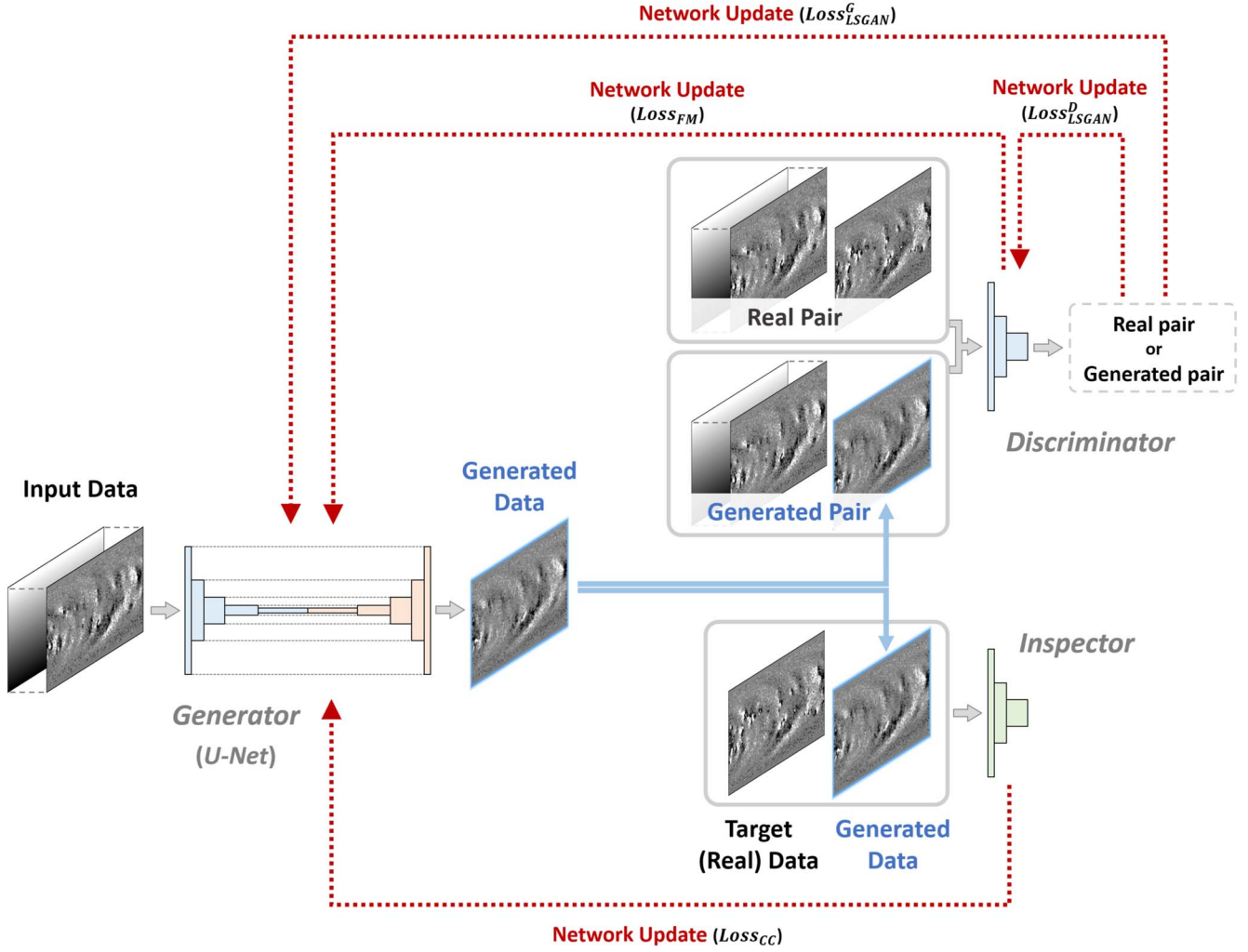
Figure 2. Flowchart and structures of our deep-learning model based on the Pix2PixCC. The generator produces target-like data from input data. The discriminator trains to distinguish between the real pair (input and target data) and the generated pair (input and AI-generated data). The inspector computes concordance CCs between the target data and generated data. The generator's parameters are updated from the losses calculated by the inspector and discriminator during the model-training process.

help of $\mathcal{L}_{CC}$, we avoid enforcing artificial saturation limits on our model.

The final objective functions are

$$\min_{G}(\lambda_1\mathcal{L}^{G}_{LSGAN}(G, D) + \lambda_2\mathcal{L}_{FM}(G, D) + \lambda_3\mathcal{L}_{CC}(G))$$
$$\min_{D}(\mathcal{L}^{D}_{LSGAN}(G, D)), \tag{5}$$

where λ_1, λ_2, and λ_3 are hyperparameters that control the importance of $\mathcal{L}^{G}_{LSGAN}$, $\mathcal{L}_{FM}$, and $\mathcal{L}_{CC}$, respectively. We set λ_1, λ_2, and λ_3 to 2, 10, and 5, respectively, following H.-J. Jeong et al. (2022). We optimize the objective functions using the adaptive moment estimation (Adam; D. P. Kingma & J. Ba 2014) optimizer with a learning rate of 0.0002 over 1,000,000 iterations, and select the best-performing model using validation data sets based on evaluation metrics.

4. Results and Discussion

4.1. Quantitative Comparison

We evaluate the performance of our deep-learning model using three metrics: rms error (RMSE), feature similarity index

measure (FSIM), and pixel-to-pixel Pearson CC between the target data and the model-predicted data in the test data sets. The RMSE measures the average differences between each pair of corresponding pixels in the output and target data. The FSIM quantifies low-level feature similarity using phase congruency and gradient magnitude to identify the local quality of the data (L. Zhang et al. 2011). The phase congruency computes the alignment of phase and amplitude across individual frequency components in the frequency domain, and the gradient magnitude measures contrast variation. The FSIM has been widely used to evaluate how blurry, noisy, or distorted the output is compared to the target data (U. Sara et al. 2019). We compute the pixel-to-pixel CC after 10×10 binning, which results in a $10°$ resolution in longitude, to compare the large-scale structure of magnetic fields on the solar surface (T. Getachew et al. 2019). The FSIM and the pixel-to-pixel CC range from 0 to 1, where 1 represents perfect agreement.

Table 1 shows that the quantitative evaluation results of our AI-based SFT model are similar to those of the conventional SFT model and better than those of the persistent model. The persistent model is based on the assumption that the output data will be the same as the input data. The average RMSE of our model results (17.8 G) is lower than that of the conventional
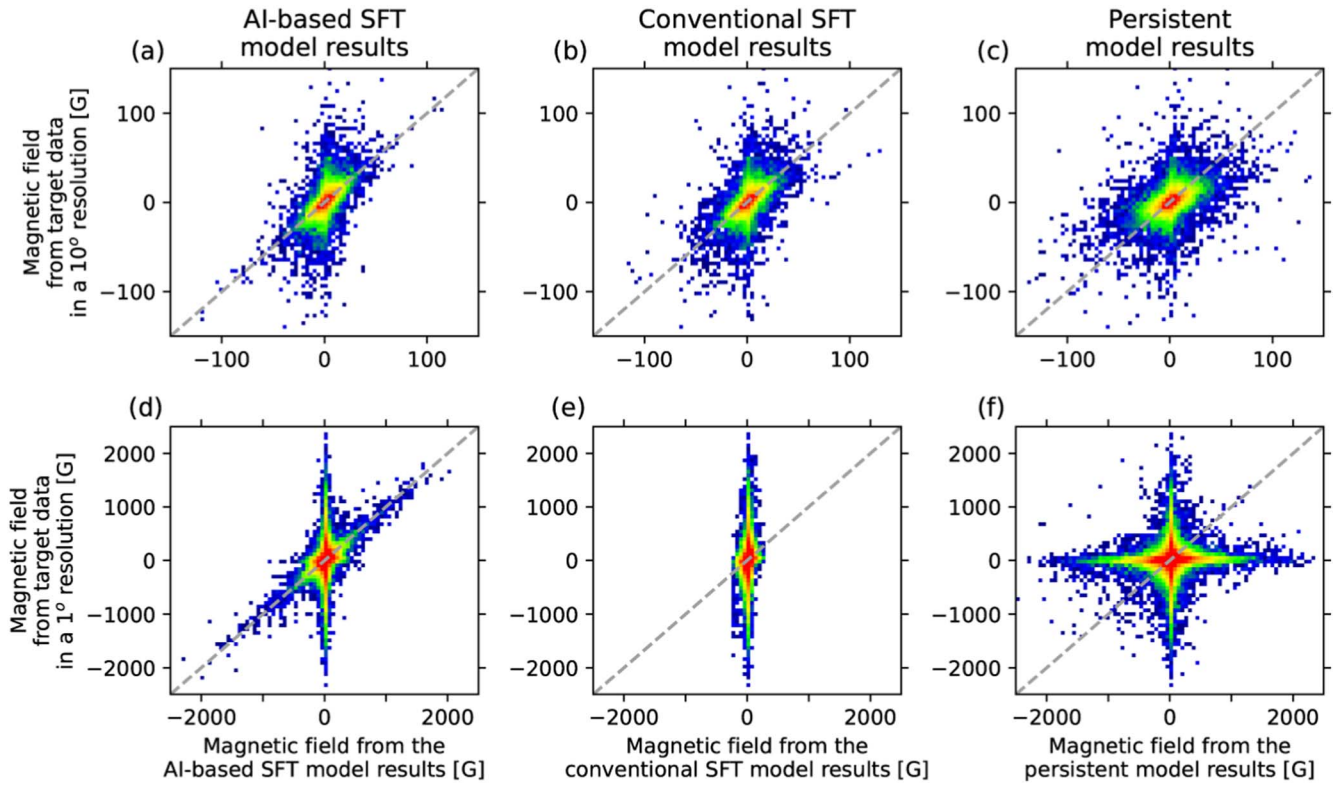
Figure 3. Comparison of pixel-to-pixel magnetic fields between target data and model results. Panels (a), (b), and (c) show scatter plots of magnetic fields from target data and results from our AI-based SFT model, the conventional SFT model, and the persistent model, respectively, in a 10° resolution. Panels (d), (e), and (f) show scatter plots of the same data in a 1° resolution. Gray dashed diagonal lines indicate positive correlations between the target's and the model's magnetic fields.

Table 1
Evaluation of Three Metric Values between Target Data and the Results of our Model, the Conventional, and the Persistent SFT Models

	RMSE (G)	FSIM	Pixel-to-pixel CC (10 × 10 Binning)
Our AI-based SFT model results	17.8	0.46	0.71
Conventional SFT model results	18.0–20.2	0.39–0.43	0.65–0.68
Persistent model results	25.1	0.42	0.56

Note. Lower RMSE values and higher FSIM and pixel-to-pixel CC values indicate better results.

SFT model results (18.0 G) and the persistent model results (25.1 G). The average FSIM and pixel-to-pixel CC of our model results (0.46 and 0.71, respectively) are higher than those of the conventional SFT model results (0.39 and 0.68, respectively) and the persistent model results (0.42 and 0.56, respectively). The average FSIM of the conventional SFT model results is lower than that of the persistent model results due to the smoothed magnetic field distributions in the conventional SFT model results. When η_H is reduced from 425 to 250 km^2 s^{-1} as suggested by R. Cameron et al. (2010), the conventional SFT model results yield the average RMSE of 19.8 G, FSIM 0.40, and pixel-to-pixel CC of 0.67. When the flux-dependent η_H is implemented, as described in J. Worden & J. Harvey (2000), the conventional SFT model results show the average RMSE of 20.2 G, FSIM of 0.43, and pixel-to-pixel CC of 0.65. As the FSIM of the conventional SFT model results increases through adjustments to the η_H parameter, its RMSE increases and pixel-to-pixel CC decreases. Our model results show higher FSIM and pixel-to-pixel CC and lower RMSE

compared to the results of three different η_H configurations for the conventional SFT model.

Figure 3 shows scatter plots of pixel-to-pixel magnetic field strengths between the target data and model results for the same data sets when calculating the average pixel-to-pixel CCs in Table 1. The results of our AI-based model and the conventional model show similar pixel-to-pixel magnetic field distributions in a 10° resolution, as shown in Figures 3(a) and (b). There are several pixels for which all three models cannot produce strong magnetic fields relative to the target data, and we expect that the reason is that these models cannot predict newly emerging magnetic fields during a solar rotation. In the case of magnetic fields generated by our model that are stronger than 200 G, the pixel-to-pixel CC shows a high value of 0.90 with the target data in a 1° resolution (Figure 3(d)). The pixel-to-pixel CCs for strong magnetic field predictions from the conventional model (Figure 3(e)) and the persistent model (Figure 3(f)) in a 1° resolution are 0.48 and 0.18, respectively.

We also train and evaluate our model separately using data sets from HMI, MDI, and GONG, and the average results from
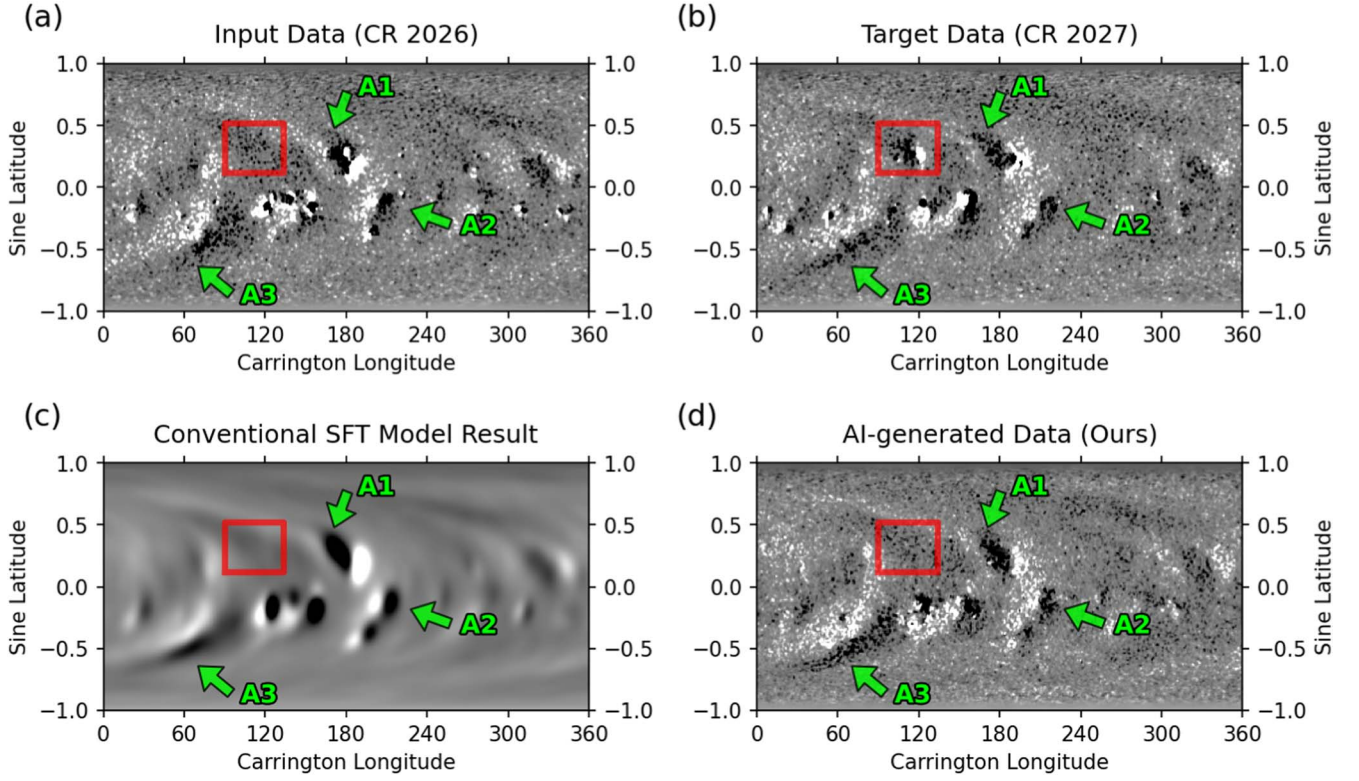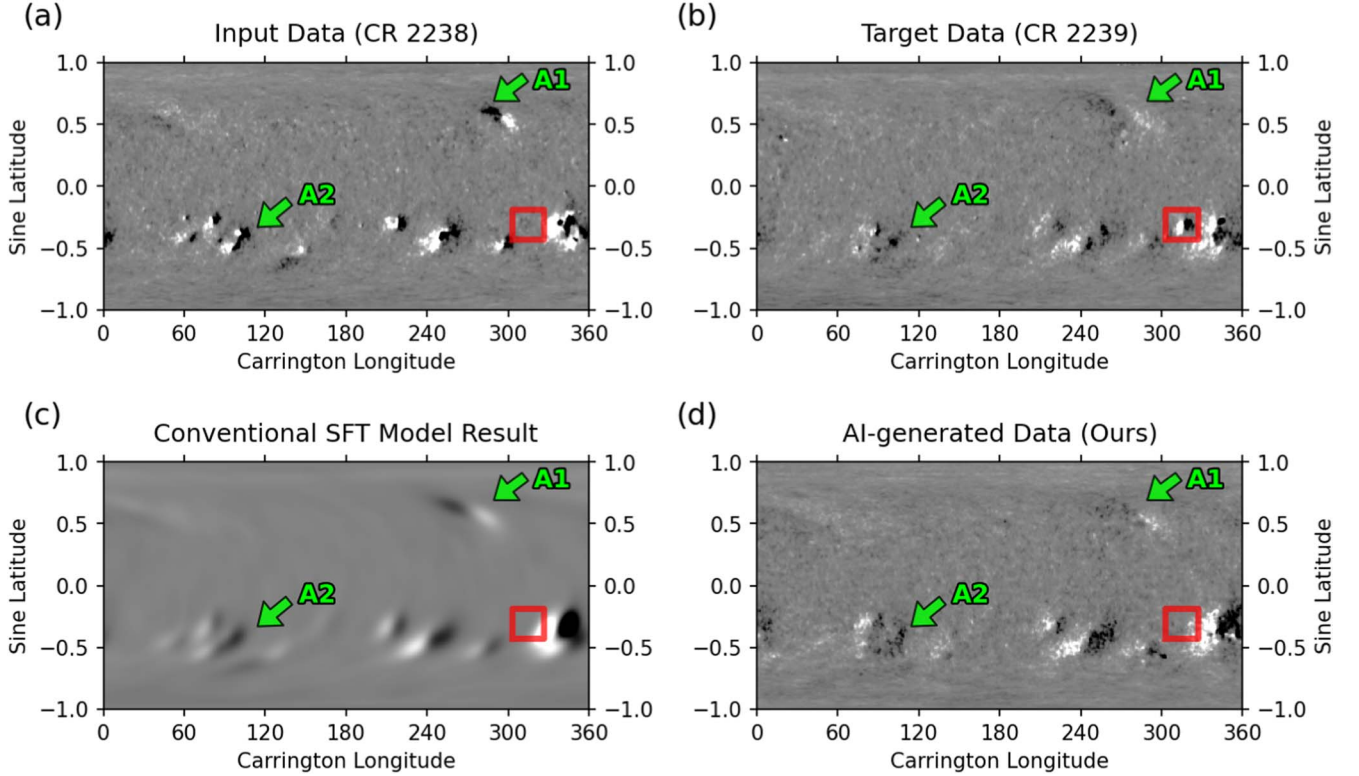
Figure 4. Comparison between MDI synoptic maps for CR 2026 (the model input) and CR 2027 (target), a conventional SFT model result, and our AI-generated data for the next solar rotation. (a)–(b) The MDI synoptic maps are input (a) and target data (b) for our deep-learning model. (c) Conventional SFT model result for the next solar rotation from the input data. (d) Our AI-generated data from the input data. Green arrows A1, A2, and A3 in (a)–(d) indicate the transported magnetic fluxes during a solar rotation, respectively. Red boxes in (a)–(d) show the location of a newly emerging active region.

Figure 5. Comparison between GONG synoptic maps for CR 2238 (the model input) and CR 2239 (target), a conventional SFT model result, and our AI-generated data for the next solar rotation. Each column, green arrows and red boxes are the same as in Figure 4.
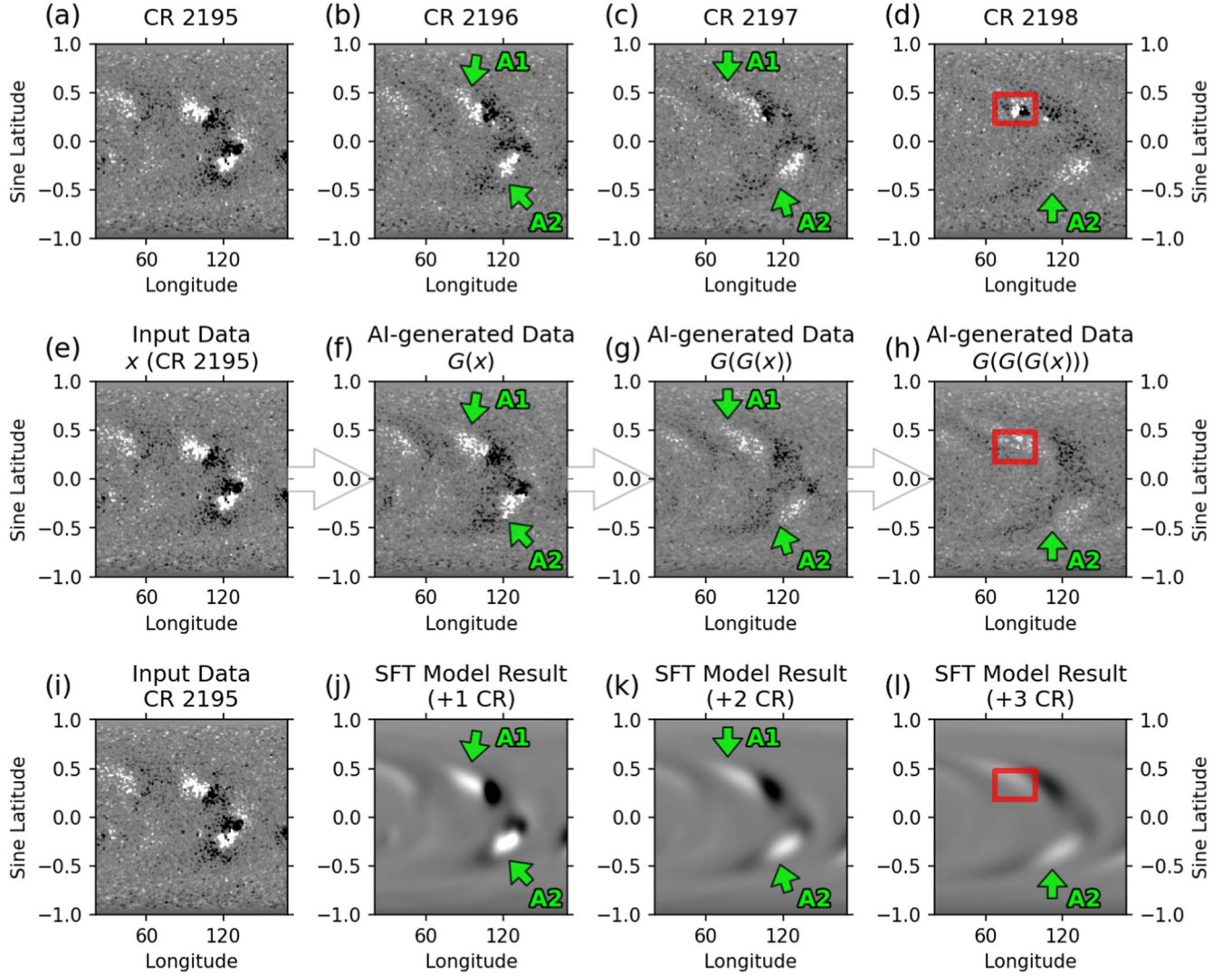
Figure 6. A series of synoptic maps, our AI-generated data, and conventional SFT model results for three solar rotations. (a)–(d) HMI synoptic maps from CR 2195 (the model input) to CR 2198 (target). (e) HMI synoptic map for CR 2195, which is input data for our deep-learning model. (f)–(h) Iteratively generated data by our deep-learning model from the input data. (i) HMI synoptic map for CR 2195, which is an input data of the conventional SFT model. (j)–(l) A series of the SFT model results for three solar rotations. Green arrows and red boxes are the same as in Figure 4.

these data sets are mostly consistent with those in Table 1. In addition, we attempt to predict the next solar rotation synoptic maps by including synoptic maps from the last one and two solar rotations as additional model inputs, but this does not lead to significant improvements. The evaluation results of the conventional SFT model might be improved by incorporating the Air Force Data Assimilative Photospheric Flux Transport (K. S. Hickmann et al. 2015) model, which employs stochastic diffusion and data assimilation methods to reproduce more realistic magnetic features, and the Advective Flux Transport (L. Upton & D. H. Hathaway 2013) model, which utilizes vector spherical harmonics to replicate the characteristics of convective flows observed on the Sun.

4.2. Qualitative Comparison

We compare the results of our AI-based SFT model with the input and target data and the results of the conventional SFT model. Figure 4 shows the data and model results for MDI synoptic maps in early 2005. The input data corresponds to the MDI synoptic map for CR 2026, and the target data is the MDI

synoptic map for the next solar rotation (CR 2027). Our AI-generated data produces the differential rotation and poleward flow of magnetic fields during a solar rotation well, as indicated by the green arrows (A1, A2, and A3) in Figure 4. Compared to the conventional SFT model result, our model result shows that magnetic field distributions and features are much closer to the target data. Our model, the conventional SFT model, and the persistent model cannot predict the appearance of a new active region (red box in Figure 4(b)) during the solar rotation.

Figure 5 shows the results when the model input is a GONG synoptic map for CR 2238 at the end of 2020. However, as in the previous case, none of the models—including ours, the conventional SFT model, and the persistent model—can predict the newly emerging active region (red box in Figure 5). While both our model and the conventional SFT model produce similar large-scale magnetic field distributions, our model generates small-sale magnetic features that are closer to the target data.

We can predict magnetic field data for several solar rotations ahead by running our model iteratively. Figure 6 shows HMI synoptic maps from CR 2195 to CR 2198 and the corresponding model results based on the input data for CR 2195.
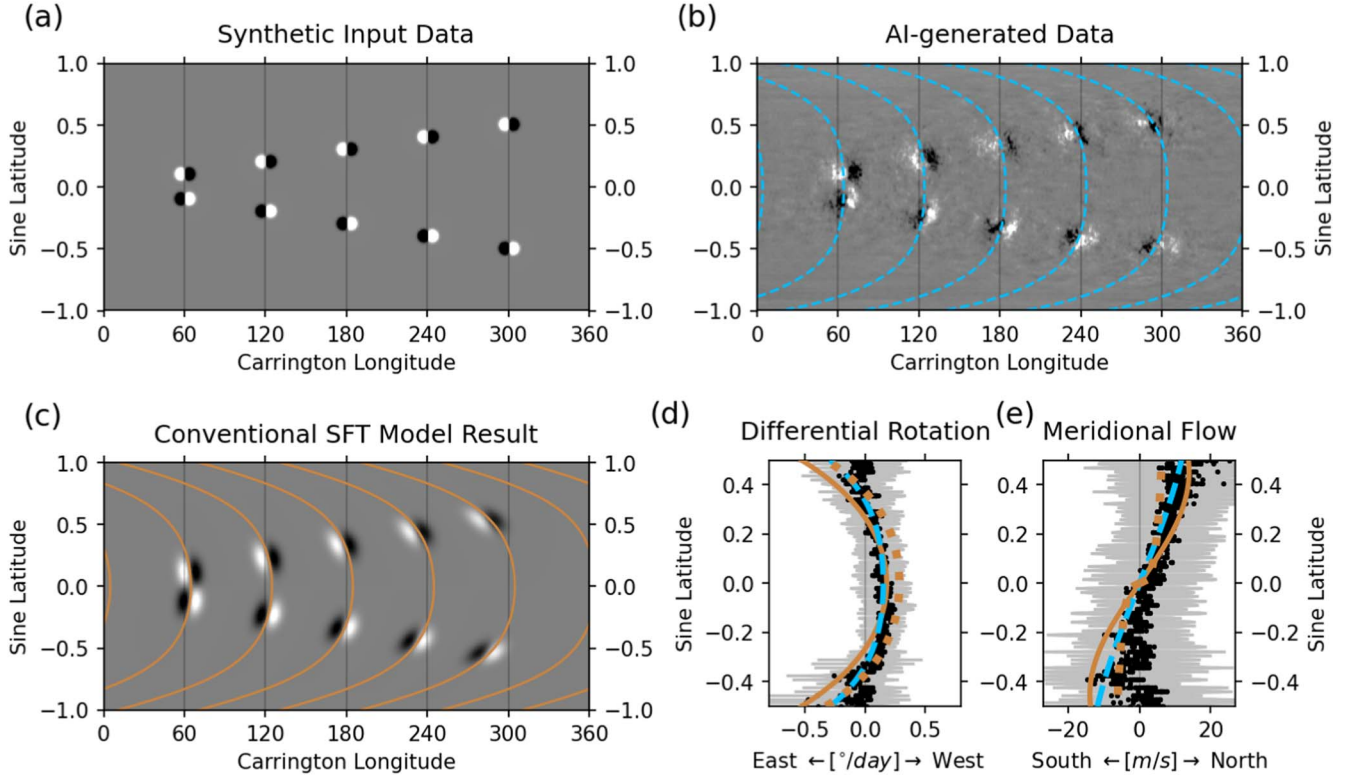
Figure 7. AI-generated data from synthetic magnetic field data and comparison with the conventional SFT model results. (a) Examples of synthetic 10 bipoles' data from −0.5 to 0.5 sine latitude and from 60° to 300° longitude at regular intervals. (b) AI-generated data from the synthetic input data. (c) Conventional SFT model result for the next solar rotation from the synthetic input data. (d)–(e) Differential rotation and meridional flow speed estimated by our AI-generated data. Blue dashed lines in (b), (d), and (e) show profiles of the SFT by our deep-learning model. Brown lines in (c)–(e) show profiles of the SFT using the conventional SFT model. Black dots and horizontal gray bars in (d)–(e) represent the mean and standard deviation, respectively, of the estimated differential rotation speeds and meridional flow speeds, calculated within 1° latitude bins.

Using our AI-based SFT model, we first generate data for one solar rotation ahead from the model input, as shown in Figure 6(f). Next, we generate data for two solar rotations ahead using the AI-generated data, as shown in Figure 6(g), and then generate data for three solar rotations ahead in a similar manner, as shown in Figure 6(h). The sequence of results from our model shows reasonable agreement with the target data. The magnetic fields of the generated data diffuse and transport toward higher latitudes, similar to those of the target data, as indicated by the green arrows (A1 and A2) in Figure 6. Although neither our model nor the conventional SFT model can predict the appearance of the new active region for CR 2198 (red boxes in Figure 6), our model generates small-sale magnetic features that are closer to the target HMI synoptic data over the three solar rotations.

4.3. Comparison Using Synthetic Data

Here we use synthetic input data to confirm that our model represents solar SFT. The synthetic data include bipolar structures with magnetic field strengths ranging from −150 to +150 G. We make 3000 synthetic data at 10° longitude intervals from 60° to 300° and at 1° latitude intervals from −0.5 to +0.5, with two different leading magnetic field polarities for the bipolar structures. Using our AI-based SFT model, we generate data for the next solar rotation from the synthetic input data. We then calculate the longitudinal and latitudinal differences of the magnetic flux-weighted centers between the input and output data. The longitudinal differences

represent differential rotation, and the latitudinal differences indicate meridional flow.

Figure 7 shows examples of 10 bipoles as input data, spaced at 60° longitude intervals and 0.1 sine-latitude intervals, and the corresponding model results. We confirm that the differential rotation and meridional flow profiles derived from our AI-generated data exhibit reasonable agreement with the conventional SFT profiles reported in several studies. The blue dashed lines in Figure 7 are SFT profiles computed from our model outputs using all 3000 synthetic input data. The brown solid lines represent profiles from the conventional SFT model parameters described in Section 3.1, providing a comparison with our AI-based SFT model results. Our results show patterns of differential rotation and meridional flow that are similar to those produced by the conventional SFT model, as shown in Figures 7(d) and (e), respectively. The brown dashed line in Figure 7(d) represents the empirical differential rotation profile measured from ephemeral regions observed during solar cycle 24 (A. S. Kutsenko 2021). The brown dashed line in Figure 7(e) shows the meridional flow profile implemented by the SFT model of C. J. Schrijver & A. M. Title (2001) and K. S. Hickmann et al. (2015).

We examine our AI-based SFT model using synthetic input data that include anomalous bipolar structures, which do not obey Hale's polarity law (G. E. Hale & S. B. Nicholson 1925) or Joy's tilt law (G. E. Hale et al. 1919). As shown in Figure 8, our model predicts the overall magnetic field distribution one solar rotation later from the anomalous bipole synthetic data, similar to the results of the conventional SFT model. The
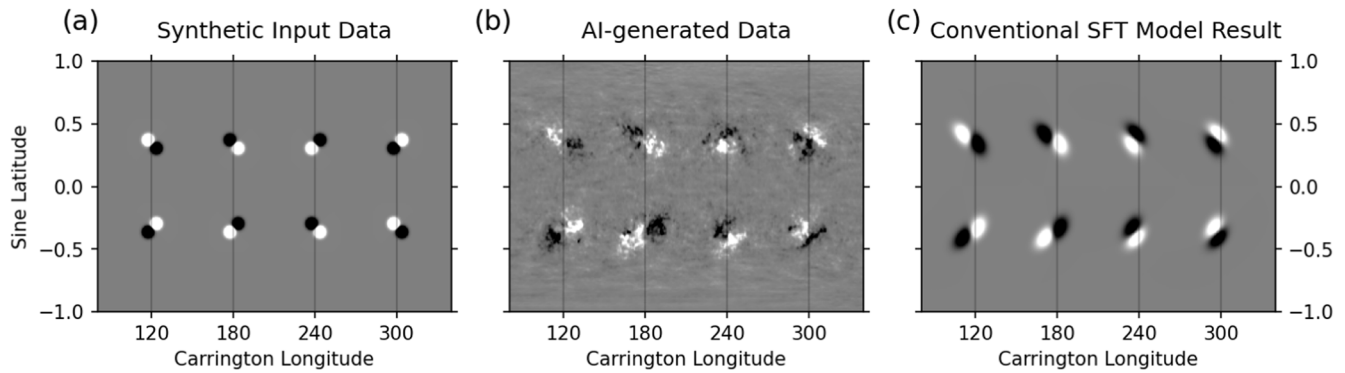
Figure 8. Comparison of our AI-generated data and the conventional SFT model results from synthetic input data, including bipolar structures with different orientations and polarities in the four configurations (Hale, anti-Hale, Joy, and anti-Joy regions) in each hemisphere. Panels (a), (b), and (c) show the synthetic input data, the results of our AI-based SFT model, and the results of the conventional SFT model, respectively.

anomalous active regions cause significant changes in large-scale solar polar field buildup and open magnetic flux dynamics during a solar cycle (J. Jiang et al. 2014; S. Pal et al. 2023). We expect that our AI-based SFT model can handle the diversity of observed solar surface field evolution dynamics and is useful for predicting the evolution of magnetic fields in both standard and anomalous bipolar regions.

5. Summary and Conclusion

In this study, we have developed an AI-based SFT model to predict the evolution of solar magnetic fields during a CR. We trained and evaluated a deep-learning model based on the Pix2PixCC architecture using SDO/HMI, SOHO/MDI, and NSO/GONG synoptic maps spanning 1996–2023. Our AI-based SFT model generates magnetic field distributions for the next solar rotation, similar to the conventional SFT model and better than the persistent model in quantitative metrics such as RMSE, FSIM, and pixel-to-pixel CC. Our AI-based model offer a useful method for quick predictive assessment. Using test and synthetic data sets, we demonstrated that our model successfully implements key SFT motions, such as differential rotation and meridional flow on the solar surface. Our model also generates small-scale magnetic features better than the conventional SFT models. Our model enables iterative forecasting over three solar rotations, showing reasonable agreement with observed data. However, like the conventional SFT model and the persistent model, predicting the magnetic fields of newly emerging active regions remains challenging for our AI-based SFT model. The predictive capability of the conventional SFT model comes from the memory inherent in the slow solar surface flow processes, assuming no significant new emergences (D. Nandy et al. 2018; S. Dash et al. 2020). We expect that this inherent memory allows our AI-based model, which is trained using more than 25 yr of synoptic maps, to predict the magnetic fields of the next solar rotation similar to the results of the conventional SFT model.

Our results can be used as initial boundary conditions for solar coronal and heliospheric numerical models, potentially enhancing space-weather forecasting from several days to months in advance. Conventional SFT model results have been utilized to predict global coronal structures (D. Nandy et al. 2018), solar extreme ultraviolet irradiance (C. Henney et al. 2015), solar wind speeds (G. Barnes et al. 2023), upcoming solar activity cycles (P. Bhowmik & D. Nandy 2018), etc. We expect that our AI-generated data would provide improved predictive outcomes for

these applications. However, we acknowledge the limitations of our method in predicting emerging magnetic fluxes of active regions, which makes it challenging to apply our AI-generated data to solar flare forecasts and extreme space-weather predictions during solar maximum. We expect that using input data with shorter time intervals (L. Bai et al. 2021; F. P. Ramunno et al. 2024) or additional data on convective motion below the solar surface (R. H. Cameron et al. 2012) may enhance our model's predictions of emerging magnetic fluxes. We leave this to future work. Our study shows a possibility that the AI-based model may show better results than existing empirical models. Furthermore, our new methodology, which uses a well-trained AI-based model and synthetic input data, can be applied to estimate empirical profiles from two-dimensional observations.

ORCID iDs

Hyun-Jin Jeong ⑩ https://orcid.org/0000-0003-4616-947X
Mingyu Jeon ⑩ https://orcid.org/0009-0004-7798-5052
Daeil Kim ⑩ https://orcid.org/0009-0008-5566-6084
Youngjae Kim ⑩ https://orcid.org/0009-0009-2316-3658
Ji-Hye Baek ⑩ https://orcid.org/0000-0002-0230-4417
Yong-Jae Moon ⑩ https://orcid.org/0000-0001-6216-6944
Seonghwan Choi ⑩ https://orcid.org/0000-0002-1946-7327

References

Athalathil, J. J., Vaidya, B., Kundu, S., Upendran, V., & Cheung, M. C. 2024, ApJ, 975, 258
Atmaja, B. T., & Akagi, M. 2021, JPhCS, 1896, 012004
Bai, L., Bi, Y., Yang, B., et al. 2021, RAA, 21, 113
Barnes, G., DeRosa, M. L., Jones, S. I., et al. 2023, ApJ, 946, 105
Bastos, B. Q., Oliveira, F. L. C., & Milidiu, R. L. 2021, Int. J. Forecast., 37, 949
Bhowmik, P., & Nandy, D. 2018, NatCo, 9, 5209
Cameron, R., Jiang, J., Schmitt, D., & Schüssler, M. 2010, ApJ, 719, 264
Cameron, R. H., Schmitt, D., Jiang, J., & Işık, E. 2012, A&A, 542, A127
Dash, S., Bhowmik, P., Athira, B., Ghosh, N., & Nandy, D. 2020, ApJ, 890, 37
Getachew, T., Virtanen, I., & Mursula, K. 2019, ApJ, 874, 116
Gosain, S., Pevtsov, A., Rudenko, G., & Anfinogentov, S. 2013, ApJ, 772, 52
Hale, G. E., Ellerman, F., Nicholson, S. B., & Joy, A. H. 1919, ApJ, 49, 153
Hale, G. E., & Nicholson, S. B. 1925, ApJ, 62, 270
Harris, C. R., Millman, K. J., Van Der Walt, S. J., et al. 2020, Natur, 585, 357
Henney, C., Hock, R., Schooley, A., et al. 2015, SpWea, 13, 141
Hickmann, K. S., Godinez, H. C., Henney, C. J., & Arge, C. N. 2015, SoPh, 290, 1105
Hoeksema, J. T., & Scherrer, P. H. 1986, SoPh, 105, 205
Howard, R., Bumba, V., & Smith, S. F. 1969, Atlas of Solar Magnetic Fields (Washington, DC: Carnegie Institution)
Hunter, J. D. 2007, CSE, 9, 90
Jeong, H.-J., Moon, Y.-J., Park, E., & Lee, H. 2020, ApJL, 903, L25
Jeong, H.-J., Moon, Y.-J., Park, E., Lee, H., & Baek, J.-H. 2022, ApJS, 262, 50
Jiang, J., Hathaway, D., Cameron, R., et al. 2014, SSRv, 186, 491
Kingma, D. P., & Ba, J. 2014, arXiv:1412.6980
Kutsenko, A. S. 2021, MNRAS, 500, 5159
Lin, L. I.-K. 1989, Biometrics, 45, 255
Lee, S., Ji, E.-Y., Moon, Y.-J., & Park, E. 2021, SpWea, 19, e2020SW002600
Leighton, R. B. 1964, ApJ, 140, 1547
Mackay, D. H., & Yeates, A. R. 2012, LRSP, 9, 1
Mao, X., Li, Q., Xie, H., et al. 2017, in 2017 IEEE Int. Conf. on Computer Vision (Piscataway, NJ: IEEE), 2813
Marnerides, D., Bashford-Rogers, T., & Debattista, K. 2021, Senso, 21, 4032
Nandy, D., Baruah, Y., Bhowmik, P., et al. 2023, JASTP, 248, 106081
Nandy, D., Bhowmik, P., Yeates, A. R., et al. 2018, ApJ, 853, 72
Owens, M. J., Horbury, T., Wicks, R., et al. 2014, SpWea, 12, 395
Pal, S., Bhowmik, P., Mahajan, S. S., & Nandy, D. 2023, ApJ, 953, 51
Park, E., Moon, Y.-J., Lee, J.-Y., et al. 2019, ApJL, 884, L23
Paszke, A., Gross, S., Massa, F., et al. 2019, in Advances in Neural Information Processing Systems 32, ed. H. Wallach et al. (NeurIPS), https://papers.neurips.cc/paper_files/paper/2019/hash/bdbca288fee7f92f2bfa9f7012727740-Abstract.html
Price-Whelan, A. M., Sipőcz, B., Günther, H., et al. 2018, AJ, 156, 123
Qiang, Y., Fei, S., Jiao, Y., & Li, L. 2020, JPhCS, 1627, 012014
Rahman, S., Shin, S., Jeong, H.-J., et al. 2023, ApJ, 948, 21
Ramunno, F. P., Jeong, H.-J., Hackstein, S., et al. 2024, arXiv:2407.11659
Rana, A., Singh, P., Valenzise, G., et al. 2019, ITIP, 29, 1285
Robitaille, T. P., Tollerud, E. J., Greenfield, P., et al. 2013, A&A, 558, A33
Ronneberger, O., Fischer, P., & Brox, T. 2015, Medical Image Computing and Computer-assisted Intervention–MICCAI 2015 (Cham: Springer), 234
Sara, U., Akter, M., & Uddin, M. S. 2019, J. Comput. Commun., 7, 8
Schrijver, C. J., & Title, A. M. 2001, ApJ, 551, 1099
Shorten, C., & Khoshgoftaar, T. M. 2019, J. Big Data, 6, 1
Snodgrass, H. B., & Ulrich, R. K. 1990, ApJ, 351, 309
Sun, X., Liu, Y., Hoeksema, J., Hayashi, K., & Zhao, X. 2011, SoPh, 270, 9
The SunPy Community, Barnes, W. T., Bobra, M. G., et al. 2020, ApJ, 890, 68
Upton, L., & Hathaway, D. H. 2013, ApJ, 780, 5
Vallejos, R., Pérez, J., Ellison, A. M., & Richardson, A. D. 2020, SpaSt, 40, 100405
Van der Walt, S., Schönberger, J. L., Nunez-Iglesias, J., et al. 2014, PeerJ, 2, e453
Vieira, L. E. A., & Solanki, S. K. 2010, A&A, 509, A100
Virtanen, P., Gommers, R., Oliphant, T. E., et al. 2020, NatMe, 17, 261
Whitbread, T., Yeates, A., Muñoz-Jaramillo, A., & Petrie, G. 2017, A&A, 607, A76
Worden, J., & Harvey, J. 2000, SoPh, 195, 247
Yeates, A. R., Cheung, M. C., Jiang, J., Petrovay, K., & Wang, Y.-M. 2023, SSRv, 219, 31
Zhang, L., Zhang, L., Mou, X., & Zhang, D. 2011, ITIP, 20, 2378